PREDICTION OF SUPERCOOLED DROPLET IMPINGEMENT ON HELICOPTER ROTOR BLADES

Krzysztof Szilder, Hongyi Xu
Institute for Aerospace Research, National Research Council
Ottawa, ON, K1A 0R6, Canada

Keywords: *icing, rotorcraft aerodynamics, CFD*

Abstract

In this paper, we describe the results of a numerical model of supercooled droplet, time-dependent trajectories and impingement on an isolated four-bladed rotor of a Bell 412 helicopter, in ideal hover flow condition. Rotor-fuselage aerodynamic interaction has been neglected in this exploratory research. The unsteady rotor flow field was obtained using CFD-FASTRAN solver and the Euler equations were used as the governing equations. This assumption significantly alleviates the grid density requirement near the surfaces and therefore greatly reduces the CPU time and memory needed for the simulation. The Chimera moving grid technique was applied to represent the blade rotation. Flow visualization was used to illustrate the prominent rotor downwash and the strong swirling flow field generated by the rotor blades. In the next step, supercooled droplets were inserted into the time-dependent, three-dimensional airflow and droplets trajectories were computed using a Lagrangian approach. The patterns of droplet impingement on rotating blades were examined for two droplet diameters. This is a first step towards predicting ice formation on rotating helicopter blades.

1 Introduction

Ice formation on components of fixed and rotary-wing aircraft can often be hazardous. In particular, icing on wings and engines of fixed-wing aircraft and on helicopter rotor blades can compromise aircraft safety. Ice deposits can degrade the aerodynamic performance of fixed and rotary wing aircraft, due to a reduction in lift and an increase in drag. However, ice forming on helicopter rotor blades is particularly dangerous, because the rotor blades can become significantly unbalanced when ice is shed, leading to severe vibrations. In addition, large pieces of shed ice can impact the aft airframe or tail rotor, with potentially hazardous consequences. Research into ice accretion on helicopter rotor blades is very active. Some experimental results are described in [1] while numerical investigations may be found in [2, 3]. The objective of the research described in this paper is to develop a predictive capability for ice formation on helicopter rotor blades. The paper deals with two elements: (1) the methodology to predict the airflow induced by rotating blades; (2) an algorithm to predict impingement of supercooled droplets on rotating blades. These two components will be described and the results of a numerical analysis will be presented and discussed.

The aerodynamics of rotary-wing flight vehicles involves a variety of complex flow phenomena, which present a grand challenge to the rotorcraft CFD community. These complex flows include: (1) transonic flow near the blade-tip, particularly on the advancing blade; (2) dynamic stalls on the retreating blade; (3) blade-tip vortices and their interactions; (4) strong flow interactions between the rotor and the fuselage. Since these flow phenomena govern the performance of a rotary-wing flight vehicle, it is crucially important to understand the physics behind these flows and to predict the phenomena based on an appropriate analytical model. So far, the advancement of computing technologies, both in terms of numerical algorithms and computer architectures, has

enabled the rotorcraft CFD community to successfully predict the attached subsonic/transonic rotor flows based on an Euler or Reynolds-Averaged Navier-Stokes (RANS) model [4]. A variety of other complex phenomena, most of them related to unsteady separation and turbulence, are yet to be satisfactorily resolved, and more advanced next-generation CFD models, such as Detached Eddy Simulation (DES) or Large Eddy Simulation (LES), are projected to play an important role in future research activities.

Aside from modelling the complicated flow physics, the rotorcraft CFD community also has to face the unique challenge of grid generation in modelling rotorcraft flow. Due to the rotor blade rotation and the associated cyclic pitch, flap and lead-lag motions, a conventional multi-block grid with a fixed-grid topology would be difficult to apply for meshing around the moving blades. In this regard, the Chimera moving grid technique, introduced by Steger et al. [5], provided the rotorcraft CFD community with an ability to generate well-formed grids, capable of resolving the near-wall boundary layer of a rotor blade, without losing the flexibility of prescribing the complex blade motions.

A few years ago, the rotary-wing program at the Aerodynamics Laboratory of NRC-IAR launched a Helicopter Modelling and Simulation project. One aim of this project was to build an unsteady simulation capability for flow past a helicopter. The CFD-FASTRAN [6] package was selected as the platform for development. This includes the grid generator CFD-GEOM and the data post-processor CFD-VIEW. Since the inception of this system at NRC, the Chimera moving grid capability in the package has been comprehensively explored and carefully tested for a number of rotor configurations, see for example [7].

In the present work, the airflow solution computed using CFD-FASTRAN, is used to compute supercooled droplet trajectories using a Lagrangian approach. It is assumed that the cloud droplets are spherical and that they do not disturb the airflow. The only force considered to act on the droplets is the aerodynamic drag arising from their motion relative to the airstream. The equations of droplet motion used in our model are similar to those used in other models [8]. Solving for droplet trajectories yields the droplet impingement pattern on rotating blades.

In the next step, we plan to predict ice formation on rotating blades. A knowledge of how to compute droplet impingement on rotor blades, together with airflow and heat transfer conditions will be the input to a unique ice accretion model developed at NRC. The model is based on a discrete particle approach, which has the ability to predict the shape, structural details and physical properties of ice accretions, by emulating the behaviour of individual fluid elements. In the past few years, it has been shown that this approach, which was originally developed to simulate ice accretion on transmission lines due to freezing rain, can also be successfully applied to the simulation of in-flight icing [9]. Recently, we have also shown that our model can be successfully used to predict ice accretion on a helicopter fuselage in forward flight conditions [10]. We have also successfully simulated three-dimensional, discrete rime structures forming on swept wings, under conditions where experiments produce ice structures called “lobster tails” or “scallops” [11]. The prediction of the ice shape and mass distribution along a rotor span is the subject of an ongoing research program at NRC.

2 Time-Dependent Numerical Model

Since the rotor aerodynamics dominates the flow past a helicopter, we decided to study first the performance of the isolated rotor in ideal hover flight conditions. This will help to understand the flow past the real helicopter, where a complex interaction between rotor induced flow and the fuselage occurs.

Figure 1 depicts the Chimera grid topologies for the isolated Bell 412 four-bladed rotor used in the computations. The C-H grid around each of the four blades is structured with two-blocks embedded in the background cylindrical grid. The grid size is $I \times J \times K = 67 \times 20 \times 44$ for each block, with a total of 59 mesh points distributed along the profile of the blades in the chord-wise direction. The background grid contains two half cylindrical

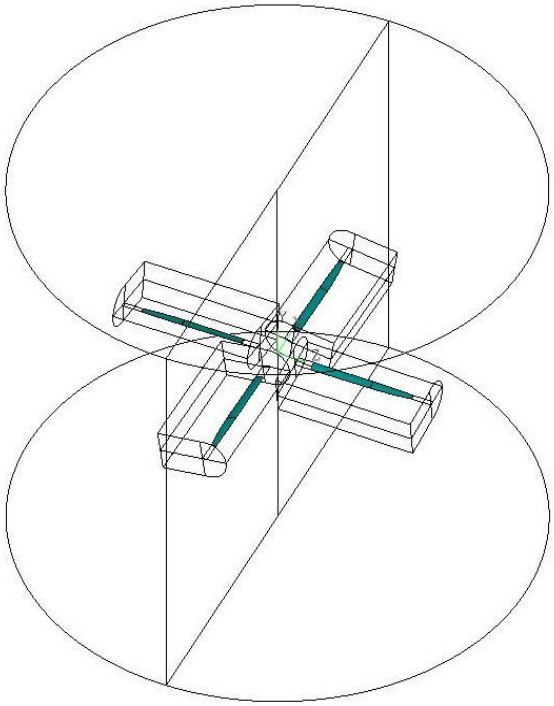

Fig. 1. Grid topologies of the Bell 412 isolated rotor.

domains, 25 m in diameter and 20 m in height. Fifty points were used in the radial direction, sixty points in the circumferential direction and fifty nine points in the vertical direction. In these exploratory computations, the rotor was assumed to be under a hover flow condition, with a blade collective pitch angle of 6 degrees. No blade cyclical motion was considered in the current investigation.

The time-dependent, three-dimensional rotor flow field, which is the output from the flow field solver, was used as input to the droplet trajectory solver. The airflow solver provided values of the velocity components, discretized in space and time. However, to compute droplet trajectories and impingement, values of flow velocity are required between grid locations and time frames. To overcome the spatial discretization issue, the velocity components at a given location were computed as a weighted average of the values at the eight grid points surrounding the point where the droplet velocity is needed. The weightings were proportional to the inverse distance between the droplet and the grid point. To resolve the time discretization problem, a linear interpolation between two neighbouring time frames was

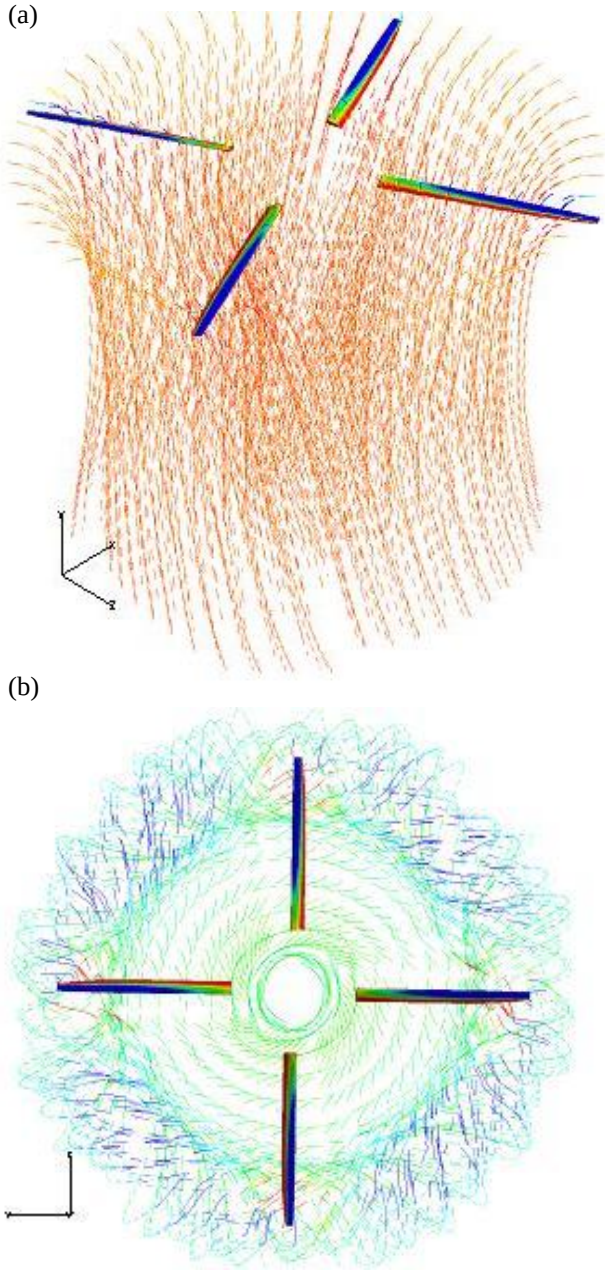

Fig. 2. Isolated rotor flow field in hover.
(a) side view; (b) top view

used to compute the velocity at a specific location and time. Since the rotation period is 0.18516 s and the time frames used for the trajectory calculation are every 9 degrees of rotation, the time increment between two time frames is 0.004629 s. In order to compute droplet trajectories, a fourth-order Runge-Kutta method was implemented and the trajectory step size was taken to be 0.2 mm.

3 Model Results and Discussion

We will first examine some of the properties of the rotor-induced flow and then look at droplet trajectories and impingement. Figures 2a and 2b are visualizations of the isolated rotor flow, depicted using instantaneous streamline particles. The blade surfaces and the streamlines are colour coded by pressure with blue and red representing the lower and higher pressure, respectively. Figure 2a depicts the prominent downwash and swirling created by the rotor blade. The rotation of the blades generates the low-pressure regions on top of the blade, as seen by the colour of the blade surface and the fluid particle traces immediately above the blade. Figure 2b depicts the path of the blade-tip vortex, which features the prominent rotor effects: a relatively low pressure above the rotor plane and a higher pressure beneath the plane.

We now examine the influence of droplet diameter on droplet trajectories and their impingement on rotating blades. Two droplets diameters were chosen for this analysis: 50 and 20 μm. All other physical parameters were kept constant.

Initially the supercooled droplets were placed on the domain boundary and their initial velocity was set equal to the local air flow velocity. The large circles depict initial droplet locations on the boundary of the cylindrical computational domain in Fig. 3a for a droplet diameter of 50 μm. These initial locations were chosen so that the resulting trajectories would pass in the vicinity of the plane of blade rotation area depicted in Fig. 3a. The droplet locations at each full rotation interval are represented by circles. The impingement locations and droplet exit points from the domain are also shown. It should be kept in mind that all four blades are rotating during droplet motion and that only some of the trajectories that cross the depicted blade area actually impinge on one of the blades. All droplets were inserted into the flow at the same time (t = 0) and impingement occurred at 6.82 s and 5.85 s for the sixth and seventh trajectories respectively (counting clockwise). These time intervals correspond to approximately 36.83 and 31.59 blade rotations, respectively. The different fractional periods for these two trajectories indicate that these two droplets impinge on the neighbouring blades.

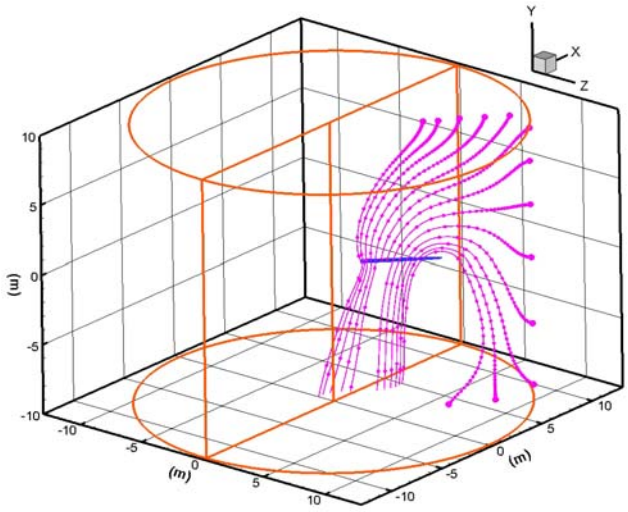

Fig. 3a. Droplet trajectories for a droplet diameter of 50 μm.

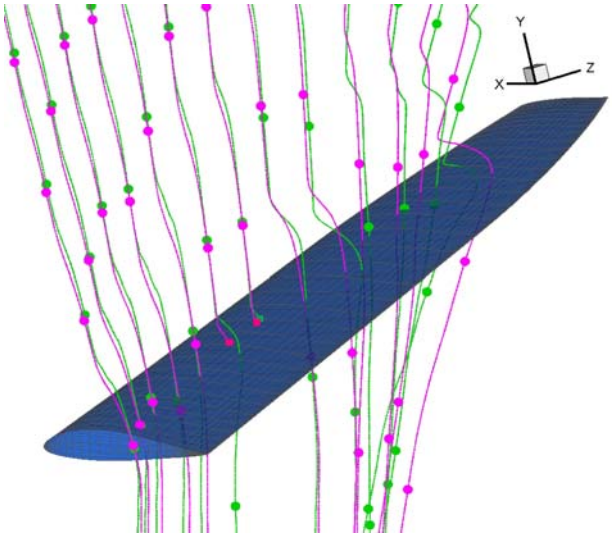

Fig. 3b. Droplet trajectories and impingement for droplet diameters of 50 (pink) and 20 (green) μm. Only some of these trajectories pass through the plane of blade rotation while the blade is at the position shown.

Figure 3b shows details of droplet trajectories in a non-rotating frame of reference for droplet diameters of 50 μm and 20 μm. All droplets are inserted simultaneously at the boundary locations displayed in Fig. 3a. The droplet locations at each one quarter rotation period are represented by circles in Fig. 3b. Also shown are two impinging trajectories for 50 μm droplets. The seventh trajectory for the 20 μm drops impinges after 5.83 s or 34.48 blade rotations. It appears that droplet diameter does not significantly influence the average droplet speed along its trajectory. It should be kept in mind that, since impingement on the rotating blades occurs at different times, the figure does not show the impingement location on the blade. This will be illustrated afterwards in a rotating frame of reference. Fig. 3b shows that droplet trajectories are almost linear close to the rotation axis, while highly erratic trajectories occur near the blade tip. The airflow is periodic over the entire domain but the greatest velocity amplitude occurs in the blade tip region, being induced by the high blade speed. Comparing the trajectories is rather difficult, due to the time dependent flow, coupled with the time lag of droplets of differing sizes. However, it may be noted that the trajectories of the smaller droplets are more complex than those of the larger droplets.

Figure 4 shows details of the 50 μm droplet trajectory impingement on the blade, including the seventh trajectory from Figs. 3a and 3b. Using the starting point of this trajectory as a base, initial coordinates were varied by ± 0.5 mm increment in the y, x and z directions (only results for y variation are shown here). The droplets were released from these locations at the same time as the central droplet and trajectories were computed. Droplets from an initial range of 14.0 mm, given by 28 trajectories, in the y direction impinge on the blade.

The impingement locations on a blade in a rotating frame of reference are depicted using red symbols. The droplets impinge not only on the upper surface of the blade but also underneath. This happens because downward moving droplets are swept out by the rapidly rotating blade. Although more droplets impinge on the upper surface, the extent of impingement on the lower surface is greater. This suggests that more ice may form on the upper surface but that the ice extent is greater on the lower surface. Analysis of the trajectories shown in Fig. 3 suggests that changing the initial droplet location along x or z, from the base location, leads to smaller numbers of impinging droplets. Computations show that droplets from an initial range of 2.5 mm in the x and z direction impinge on the blade. It may be also noted that the final impingement positions lie almost along a line determined by the starting point locations in the y direction (not shown here).

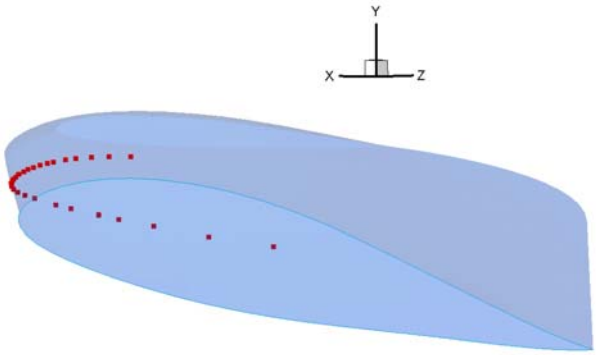

Fig 4. Location of 50μm droplet impingement on a blade in a rotating frame of reference shown for varying initial droplet location in y direction.

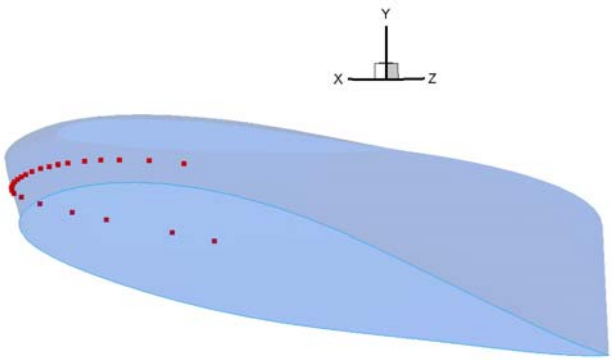

Fig 5. The same as Fig. 4 but for droplet diameter of 20 μm.

A similar analysis of droplet trajectories and impingement was performed for a droplet diameter of 20 μm, see Fig. 5. Due to their decreased inertia, trajectories for smaller droplets tend to be more responsive to variations in the airflow. Because this airflow is complex and time-dependent, especially near the blade tip, the trajectories are correspondingly more convoluted. The starting point range of the impinging droplets, in the y direction, was 12.0 mm. As in the 50 μm case, it may be deduced that more ice will form on the upper surface, but that the ice extent on the lower surface will be greater. The extent of the upper surface impingement zone increases with decreasing droplet diameter while the opposite effect is observed for lower surface. Varying the starting point in x and z leads to qualitatively similar results as for the 50 μm droplets, but fewer droplets impinge in the 20 μm case (the initial location range is 2.0 mm). The lower collision efficiency for smaller droplets is the result of a smaller departure from the streamlines with decreasing droplet inertia.

4 Conclusions

We have demonstrated in this paper that it is possible, with reasonable computational effort, to predict cloud droplet time-dependent impingement on rotating helicopter blades in hover. The CFD-FASTRAN flow solver captures most of the prominent features of rotor flows, including downwash, swirl and blade-tip vortices. A preliminary analysis indicates that more droplets impinge on the upper blade surface, and that the extent of droplet impingement is greater underneath the blade. The extent of the upper surface impingement increases with decreasing droplet diameter, while the opposite effect is observed beneath the blade. These impingement characteristics were observed close to the rotational axis.

The work presented here is a first step towards our goal of numerically simulating icing on helicopter rotors. We plan to combine droplet impingement prediction with flow and heat transfer computations in order to predict ice formation. Subsequent research will focus on the even more challenging problem of ice shedding and the potential impact of shed ice on aircraft safety.

References

[1] Flemming R J and Alldridge P J. Sikorsky S-92A and S-76D helicopter rotor ice protection systems. *SAE Aircraft & Engine Icing International Conference*, Seville, Spain, 2007-01-3299, 2007.

[2] Zanazzi G, Mingione G, Pagano A, Visingardi A and Narducci, R. Ice accretion prediction on helicopter rotor blade in hover flight. *SAE Aircraft & Engine Icing International Conference*, Seville, Spain, 2007-01-3309, 2007.

[3] Aube M S, Baruzzi G S and Habashi W G. Application of FENSAP-ICE-unsteady to helicopter icing. *SAE Aircraft & Engine Icing International Conference*, Seville, Spain, 2007-01-3310, 2007.

[4] Strawn R C, Caradonna F X and Duque E P N. 30 years of rotorcraft computational fluid dynamics research and development. *Journal of the American Helicopter Society*, pp 5-21, January 2006.

[5] Steger J L, Dougherty F C and Benek J A. A Chimera grid scheme. *American Society of Mechanical Engineers, Fluids Engineering Division (Publication) FED*, Vol. 5, 1983.

[6] *CFD-FASTRAN Software Manual*, CFD Research Corporation, Huntsville, AL, 2002.

[7] Xu H and Zhang S. Aerodynamic investigations of unsteady flow past robin helicopter with four-bladed rotor in forward flight. *32nd European Rotorcraft Forum*, Maastricht, The Netherlands, 2006.

[8] Kind R J, Potapczuk M G, Feo A, Golia C and Shah A D. Experimental and computational simulation of in-flight icing phenomena. *Progress in Aerospace Sciences*, 34, pp 257-435, 1998.

[9] Szilder K and Lozowski E P. Novel two-dimensional modeling approach for aircraft icing. *Journal of Aircraft*, Vol. 41, No. 4, pp 854-861, 2004.

[10] Szilder K. Numerical simulation of ice formation on a helicopter fuselage. *SAE Aircraft & Engine Icing International Conference*, Seville, Spain, 2007-01-3308, 2007.

[11] Szilder K, McIlwain S and Lozowski E P. Numerical simulation of complex ice shapes on swept wings. *ICAS 2006, 25th International Congress of the Aeronautical Sciences*, Hamburg, Germany, ICAS 2006-2.5.1, 2006.

Copyright Statement

the publication and distribution of their paper as part of the ICAS2008 proceedings or as individual off-prints from the proceedings.